



Influence of adipic acid on anodic film formation and corrosion resistance of 2024 aluminum alloy

Ying-dong LI^{1,2}, You ZHANG¹, Song-mei LI¹, Pi-zhi ZHAO²

1. School of Materials Science and Engineering, Beihang University, Beijing 100191, China;
2. Chinalco Research Institute of Science and Technology Co., Ltd., Beijing 102209, China

Received 5 March 2015; accepted 17 November 2015

Abstract: The influence of adipic acid on the formation and corrosion resistance of anodic oxide film fabricated on 2024 aluminum alloy was investigated. The morphology was investigated by scanning electron microscopy (SEM) and transmission electron microscopy (TEM), respectively. The corrosion resistance was evaluated by electrochemical impedance spectroscopy (EIS). The results showed that the adipic acid was absorbed at the electrolyte/anodic layer interface during anodizing. The corrosion rate of anodic film decreased and the film thickness increased. The film was uniform and compact especially at the film/substrate interface. After sealing procedure, anodic film formed with the addition of adipic acid exhibited improved dielectric property and corrosion resistance in aggressive environment.

Key words: aluminum alloy; anodic oxidation; adipic acid; adsorption; corrosion

1 Introduction

The combination of high strength and low density makes 2024 aluminum alloys suitable to be used in aeronautical industry to manufacture different structural components. However, pitting attack by forming galvanic couples easily occurs, due to the presence of alloying elements [1–4]. In practice, 2024 aluminum alloy always undergoes surface treatments to improve its corrosion resistance. Traditional chromic acid (CA) anodizing method provides outstanding corrosion resistance but is gradually substituted for environmental concerns and legal restrictions. Sulfuric acid (SA) anodizing method provides similar corrosion resistance compared with CA, but the relatively thick anodic film is brittle and easily cracks under cyclic stress [5]. Accordingly, more dilute sulfuric acid has been introduced to obtain thin anodic films which could increase fatigue resistance for specific structural materials.

In order to obtain similar corrosion resistance as traditional CA and SA, the dilute sulfuric acid anodizing electrolytes require additions of various modifiers to form enhanced protective anodic oxide film. Generally, these modifiers include inorganic acid [6,7],

organic acid [8,9], alcohol [10,11] and corrosion inhibitor [12,13].

Among these modifiers, one of the most important modifiers is carboxylic acid, especially the dicarboxylic acid such as malonic acid [14], tartaric acid [15], glutaric acid [16], malic acid [17] and oxalic acid [18]. These modifiers could significantly improve the anticorrosive property of the anodic film. However, the mechanism explaining how dicarboxylic acid improves the properties of anodic layer is still not fully understood. Some authors proposed the assumption that the added dicarboxylic acid might reduce the field-assisted dissolution of anodic film [19] or influence the viscosity of electrolyte [20]. On the other hand, CURIONI et al [21] and MARZOCCHI et al [22] suggested that tartaric acid hardly changed the morphology of the cell and pores. ARENAS et al [23] proposed a new protective mechanism that tartaric acid would remain inside the pores and chelate with Al^{3+} and Cu^{2+} cations to prevent further corrosion.

The present study aimed at a better understanding of the influence of dicarboxylic acid on the formation as well as the corrosion resistance of anodic film fabricated on 2024 aluminum alloy. The improvement mechanism was investigated by means of direct observation with scanning electron microscopy (SEM) and transmission

electron microscopy (TEM). Meanwhile, electrochemical techniques were also employed to provide further description.

2 Experimental

2024 aluminum alloy (major elements in mass fraction: 4.5% Cu, 1.44% Mg, 0.6% Mn, 0.06% Si, 0.13% Fe, 0.02% Zn, 0.03% Ti) samples with dimensions of 100 mm × 50 mm × 2 mm were used as electrode. Prior to application, the samples were mechanically ground to 2000 grit silicon carbide paper, etched in 50 g/L NaOH solution at 50 °C for 1 min, and then desmutted in 4.7 mol/L HNO₃ at room temperature for 1 min.

The anodizing process was performed with 2024 aluminum alloy plate as anode and a stainless plate as cathode. The anodizing baths include: sulfuric acid electrolyte (50 g/L sulfuric acid) and adipic/sulfuric acid electrolyte (50 g/L sulfuric acid + 10 g/L adipic acid). In brief, samples anodized in sulfuric acid electrolyte are named as SA, while those anodized in adipic/sulfuric acid electrolyte are named as ASA. During anodizing, a constant voltage of 15 V was applied and the anodizing time was 20 min. The solution was vigorously stirred to maintain the temperature at 25 °C. Sealing process was undertaken by immersion in boiling distilled water for 30 min.

The galvanostatic polarization was performed in a thermostatically controlled electrochemical cell (± 1 °C) in ASA and SA electrolytes, respectively. A three-electrode cell was used with a platinum plate auxiliary electrode, a saturated calomel reference electrode (SCE) and the tested samples (exposed area of 1 cm²) as working electrode. Electrochemical tests were carried out using a computer-controlled potentiostatic/frequency response analyzer (model Parstat 2273, AMETEK Inc.). For the conventional experiments, electrochemical impedance spectroscopy (EIS) measurements were conducted over a frequency range of 10⁵ down to 10⁻² Hz, with seven points per decade using a 10 mV sine wave with data presented as Bode plots.

The morphology of anodic films (without sealing process) was examined by scanning electron microscopy (SEM) using a Hitachi S-4800 FE-SEM operated at 15 kV. Cross sections of specimens were also prepared using ion thinner beam to a nominal thickness of 20 nm and examined on a JEM-2100F transmission electron microscope (TEM).

3 Results and discussion

3.1 Morphology characterization

Figure 1 shows the morphologies of the anodic films prepared in SA and ASA. It is shown that both

films exhibit porous structure; however, the size of pores slightly decreases with the addition of adipic acid. It is also observed that the porous structure is more regular for the sample prepared in ASA than that in SA.

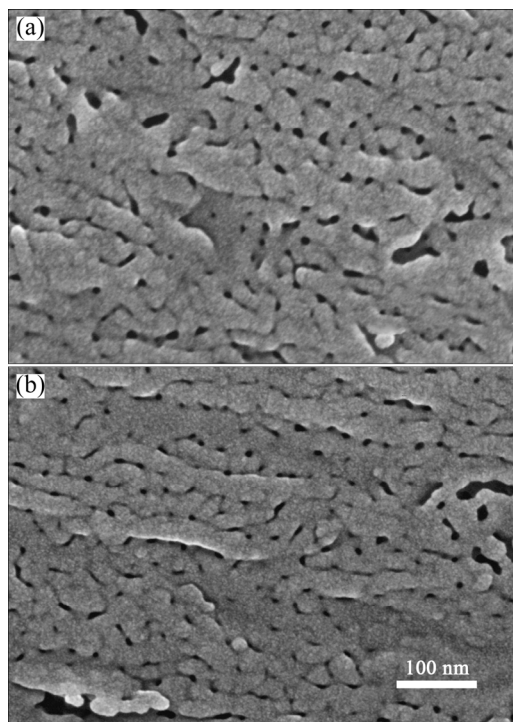


Fig. 1 SEM images of anodic films formed in SA (a) and ASA (b)

Figure 2 shows the cross section images of the anodic films. It is observed that both films are uniform in thickness, with relatively flat film/alloy and electrolyte/film interfaces. The anodic film fabricated in SA (Fig. 2(a)) exhibits looser arrangement with coarser pore channels located at film/alloy interface, while that in ASA (Fig. 2(b)) shows more compact arrangement. It is observed that the average film thickness of ASA sample is 1.93 μm , which is 0.12 μm larger than that of SA sample. The cross section images suggest that adipic acid promotes the growth of anodic film, especially improves the initial formation process.

3.2 Anticorrosive properties of hydrothermal sealed anodic films

After sealing procedure, the samples were immersed in 3.5% NaCl solution and EIS measurements were conducted to evaluate the anticorrosive properties. Figure 3 shows the Bode plots of the sealed anodic layers formed in SA and ASA. It is observed that each sample shows two well-defined time constants, which are recorded in high and medium frequency ranges (between 10² Hz and 10⁴ Hz) and low frequency range (between 10⁻¹ Hz and 10 Hz), respectively. After 336 h of immersion, zones in Bode phase plots related to the

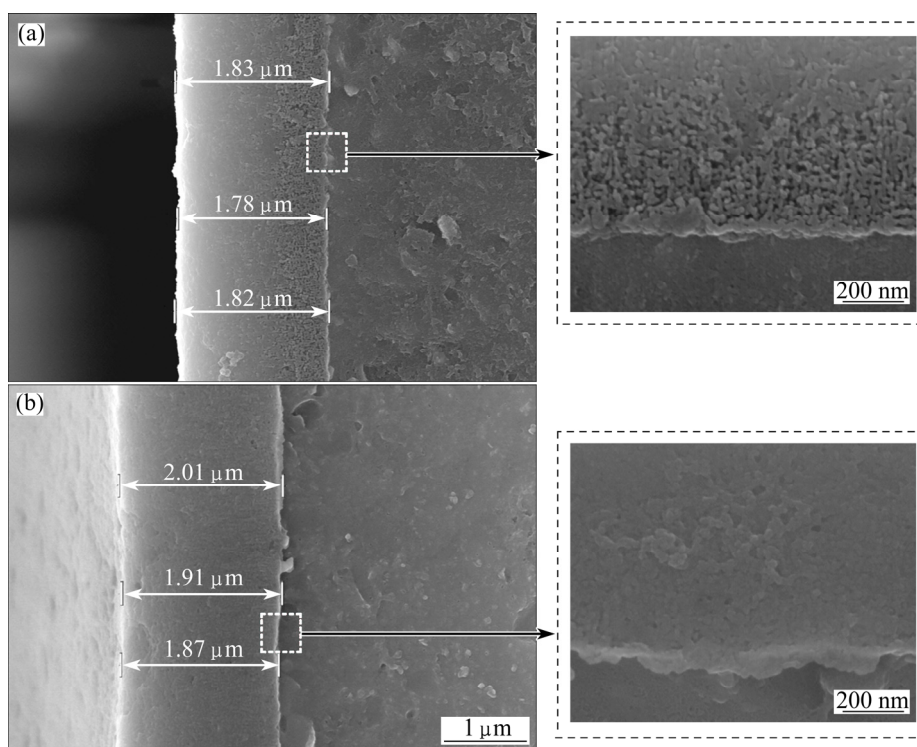


Fig. 2 Cross section SEM images of anodic layers in SA (a) and ASA (b)

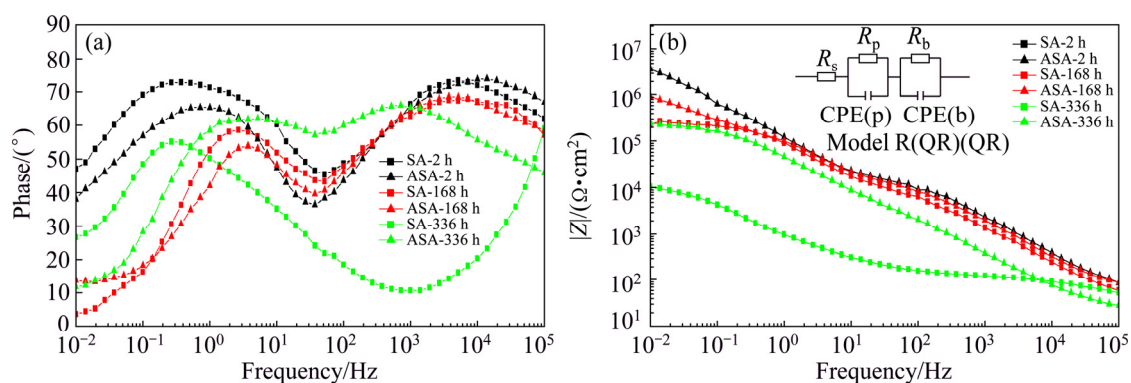


Fig. 3 Bode plots of sealed SA and ASA samples as function of immersion time

barrier layer and porous layer become close for the ASA sample. This is associated with the high conductivity of the electrolytic solution permeating into porous layer. However, a major change occurs for the SA sample, indicating that the dielectric property of the anodic layer has significantly changed. The values of impedance decrease significantly in the whole frequency ranges, probably indicating that the film structure has been destroyed by the penetration of Cl^- .

Detailed corrosion behavior during immersion could be illustrated by the equivalent circuit shown in Fig. 3(b). In this model, R_s is the electrolytic resistance, i.e., NaCl solution. Parameters concerning the porous layer are characterized by the capacitance C_p and the resistance R_p . Barrier layer properties are described by the capacitance C_b and the resistance R_b . However, porous layer and barrier layer have heterogeneities from Bode plots,

making their capacitive behavior better simulated by constant phase elements (CPE) than by simple capacitances C ($\text{CPE} = 1/C(j\omega)^\alpha$). Thus, parameters α_p and α_b affect C_p and C_b , respectively, to take into account the non-ideal capacitive behavior. Parameter α is the frequency dispersion factor and varies from 1 to 0. When $\alpha=1$, CPE can be considered as real capacitances, whereas $\alpha=0$ represents a real resistance.

Table 1 lists the parameters determined from fitting of the Bode plots with the described equivalent circuit. For the initial 2 h of immersion, the ASA sample exhibits higher value of R_p with respect to the SA sample. This is associated with the thicker porous layer of ASA sample as mentioned in Fig. 2. Meanwhile, both values of C_p and C_b of ASA sample are lower than those of SA sample, indicating that the anodic layer is more compactly arranged. After 168 h of immersion, the values of R_p and

R_b decrease, while the values of C_p and C_b increase for both samples. This means that the aggressive electrolyte has gradually penetrated into porous layer and the conductivity of the anodic films gradually increases. As the immersion time reaches 336 h, the SA sample shows significant decrease of R_b , indicating that the barrier layer has been seriously destroyed. The anodic layer fails to provide sufficient protection for the substrate after long time of immersion. However, the ASA sample still shows relatively high value of R_b , indicating that the anodic layer is still integral.

Figure 4 shows the SEM images of the samples after 336 h of immersion. It is observed that the width of cracks is about 0.7 μm for the SA sample. This is associated with the corrosion of the underlying substrate due to the penetration of aggressive Cl^- ions. The corrosion of aluminum alloy in a Cl-containing solution should include anodic dissolution of aluminum:



and cathodic hydrogen evolution:



Thus, internal stress generates during immersion, leading to the emersion of cracks. In contrast, the surface of ASA sample shows no obvious cracks although the surface is also partially corroded. This suggests that the film provides sufficient protection against the penetration

of aggressive ions, due to the compact arrangement of anodic film.

3.3 Absorption behavior of adipic acid

The characteristics of the electrode/electrolyte interface, including electron transfer, mass transport and chemical reaction, will influence the impedance of the interface. The impedance of interface depends on the texture and nature of the electrodes, the electrolyte composition and the charge of species absorbed at interface. In-situ EIS measurements are suitable for the investigation of aluminum oxide film as well as the electrochemical process at oxide film/electrolyte interface.

The galvanostatic polarization of bare 2024 aluminum alloy was applied at a current density of 1 mA/cm^2 in SA and ASA, respectively. It is observed in Fig. 5 that the potential increases rapidly at the beginning, corresponding to the formation of barrier layer. Afterwards, the potential is stable, which is associated with the growth of porous layer. The constant potential for SA sample is 3.5 V, while that for ASA sample is 3.1 V. This suggests that the presence of adipic acid helps the proton transmission in the electrolyte.

The detailed morphologies at the film/alloy interface are shown in Fig. 6. It is observed that the ASA sample shows more regular arrangement of pore channels and its pore diameter is lower than that of the SA sample. This is probably associated with the less ejection of Al^{3+} ion and dissolution of alumina due to

Table 1 Results after fitting Bode plots for samples prepared in SA and ASA as function of immersion time

Sample	Time/h	$R_p/(\text{k}\Omega \cdot \text{cm}^2)$	CPE(p)		$R_b/(\text{k}\Omega \cdot \text{cm}^2)$	CPE(b)	
			$C_p/(\mu\text{F} \cdot \text{cm}^{-2})$	α_p		$C_b/(\mu\text{F} \cdot \text{cm}^{-2})$	α_b
SA anodized	2	5.345	0.925	0.77	2850.1	1.665	0.88
	168	6.74	1.56	0.73	530.2	2.391	0.83
	336	0.193	6.24	0.58	17.0	298.6	0.80
ASA anodized	2	84	0.499	0.89	2935.8	1.021	0.83
	168	10.43	1.052	0.74	1190.3	2.145	0.85
	336	4.759	5.941	0.72	755.7	2.931	0.78

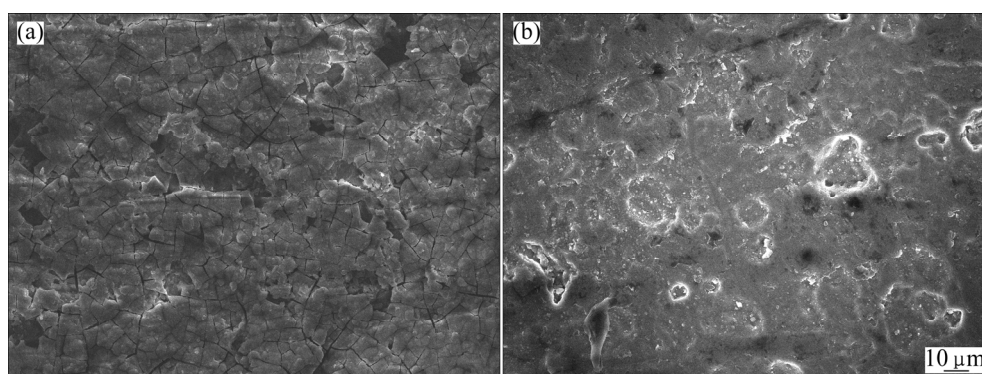


Fig. 4 SEM images of SA (a) and ASA (b) samples after 336 h of immersion

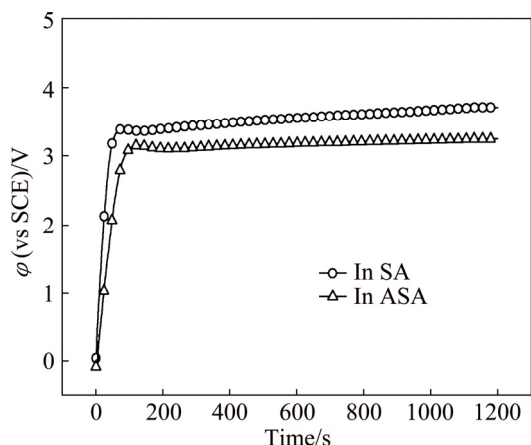


Fig. 5 Potential–time curves of aluminum alloy at 1 mA/cm² in SA and ASA, respectively

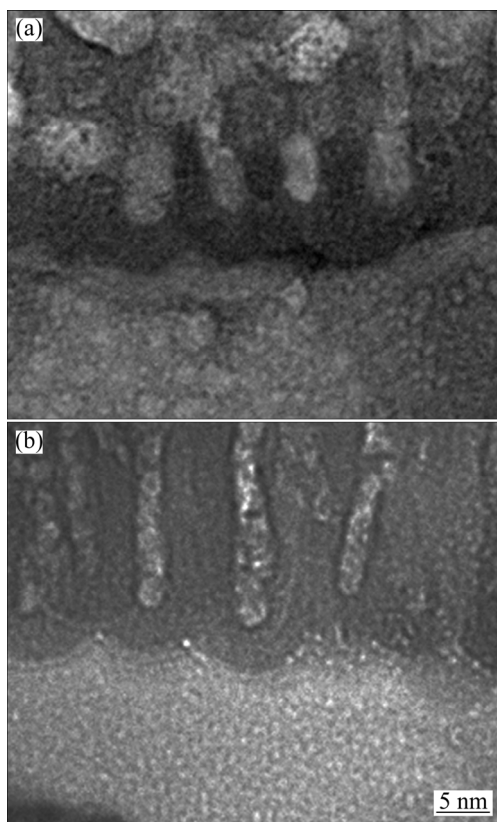


Fig. 6 TEM images of SA (a) and ASA (b) samples at film/alloy interface after galvanostatic polarization

lower electric field strength at oxide/electrolyte interface, which would lead to a higher volume expansion factor [18]. The thickness of barrier layer of SA sample is 4.6 nm, while that of ASA sample is 4.1 nm. This is consistent with the constant potential applied during galvanostatic polarization, showing a formation rate of 1.2–1.3 nm/V.

After galvanostatic polarization, the current was switched off. In-situ EIS measurements were performed at OCP after various intervals (from 15 to 120 min) to

precisely evaluate the local reactions. During immersion in anodizing bath, the anodic film would be gradually corroded by chemical dissolution [24]. This could be assumed as a procedure to thin both the porous layer and the barrier layer. However, the response of barrier layer in unsealed anodized aluminum is the main contribution to the behavior of measured system. The information of unsealed porous layer was hardly obtained, due to the short circuiting of electrolyte [25].

As shown in Fig. 7(a), the black and red plots are recorded as EIS plots for the sample after different periods of immersion in SA and ASA baths, respectively. The impedance spectra of ASA sample could be divided into two stages: 1) initially, the curve consists of one capacitive semicircle and one inductive semicircle, located in high and low frequency regions, respectively. In literature, the capacitive semicircle located in high frequency range is associated with the properties of anodic oxide film and the one located in low frequency is related to ionic relaxation phenomenon or absorption behavior [26,27]; 2) after a period of immersion

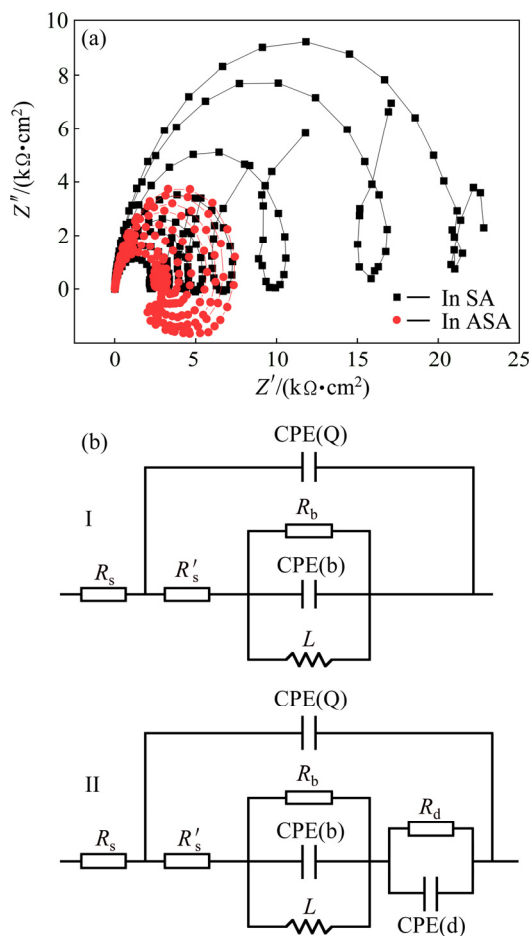


Fig. 7 Nyquist plots of sample after galvanostatic polarization (a) and equivalent electrical circuit (b) used for analysis of impedance spectra of samples ASA (Circuit I) and SA (Circuit II)

(~90 min), a second capacitance loop emerges, indicating that the anodic films gradually degenerate under aggressive electrolyte condition. Meanwhile, a new passive film emerges above the bare alloy. According to the entire Nyquist plots, the SA sample shows initial higher impedance values but a faster decrease compared with ASA sample. The initial higher value of impedance could be attributed to the thicker barrier layer observed in Fig. 6. Nevertheless, the SA sample hardly displays the first stage, suggesting that the barrier layer of SA sample is easily corroded by the electrolyte. This could be the reason for the rapid decrease of impedance values.

With the help of equivalent circuits in Fig. 7(b), the variation of the anodic film properties is further investigated. As for ASA sample, the system is simulated by Circuit I, where R_s represents the resistance of bulk electrolyte outside; R'_s refers to the resistance inside the porous layer. CPE(Q) denotes as double layer capacitance of the overall system; CPE(b) and R_b indicate the barrier layer capacitance and resistance, respectively; L being the inductance related to the inductive loop reveals that the surface area is partially or totally active [28,29]. During immersion, an appropriate circuit is presented in Circuit II when a second capacitance loop emerges, where R_d represents the resistance of charge transfer and C_d represents the capacitance of double layer. As for SA, the whole process could be simulated by Circuit II according to the shape of the impedance curves.

Table 2 lists the parameters determined from fitting

of the EIS spectra with the described equivalent circuits in Fig. 7(b). For the ASA sample, values of α_b equal 1 at the beginning, indicating that the barrier layer represents ideal capacitance, and the initial thickness of the barrier layer, d_b , could be estimated by the fitting values of C_b , according to the general expression:

$$C_b = \epsilon_r \epsilon_0 S / d_b \quad (5)$$

where ϵ_r is the relative constant for aluminum oxide and $\epsilon_r = 10$, ϵ_0 is the dielectric constant in vacuum and $\epsilon_0 = 8.854 \times 10^{-12}$ F/m, S is the surface area of the electrode and $S = 1 \text{ cm}^2$.

The calculated thickness of barrier layer is approximately 3.8 nm for ASA sample, slightly thinner than the TEM observation. Afterwards, values of α_b decrease close to 0, indicating that electrolyte has penetrated through the barrier layer to the bare alloy. However, the newly formed passive film induced by the acidic electrolyte presents ideal capacitance ($\alpha_d = 1$). It can also be seen that R_b decreases with the increase of immersion time.

The values of inductance (L) decrease with the increase of immersion time. In Ref. [27], the inductance in the proposed equivalent circuit may be related to adsorption phenomena (most probably the adsorption of SO_4^{2-} , $\text{H}_2\text{C}_6\text{H}_8\text{O}_4$, $\text{HC}_6\text{H}_8\text{O}_4^-$ and $\text{C}_6\text{H}_8\text{O}_4^{2-}$ in inner Helmholtz layer). During immersion, the Al_2O_3 layer is gradually removed and the adsorption ability of bared Al alloy is weakened due to the effect of depolarization agent, and thus, values of L decrease.

Table 2 Results after fitting Nyquist plots in Fig. 7 according to proposed equivalent electrical circuits

Mode	Time/min	CPE(Q)		$R_b/(\text{k}\Omega \cdot \text{cm}^2)$	CPE(b)		L/H	$R_d/(\text{k}\Omega \cdot \text{cm}^2)$	CPE(d)	
		$C_Q/(\mu\text{F} \cdot \text{cm}^{-2})$	α_Q		$C_b/(\mu\text{F} \cdot \text{cm}^{-2})$	α_b			$C_d/(\mu\text{F} \cdot \text{cm}^{-2})$	α_d
In SA	15	2.676	0.9708	6.076	2.194	1	8846	56.97	39.55	0.1652
	30	3.706	0.9555	4.957	6.526	1	7467	58.68	51.75	0.5614
	45	4.355	0.9613	3.528	7.023	1	3387	40.64	77.73	0.621
	60	5.727	0.9583	1.830	8.518	1	1493	41.06	26.54	0.9688
	75	7.325	0.9618	1.510	10.13	1	1288	53.78	23.67	0.7927
	90	10.18	0.9561	0.912	26.31	1	804.1	72.62	47.46	0.9391
	105	12.12	0.9671	0.875	29.23	1	721	13.43	35.62	0.6492
	120	15.64	0.9685	0.594	30.57	1	688.1	44.22	44.51	0.5383
In ASA	15	11.34	0.9125	4.573	2.303	1	4937	—	—	—
	30	16.94	0.9156	4.582	1.828	1	4213	—	—	—
	45	21.46	0.9141	4.131	1.245	1	5252	—	—	—
	60	24.61	0.914	3.303	1.399	1	4958	—	—	—
	75	27.88	0.9112	2.222	1.619	1	2679	—	—	—
	90	35.63	0.9003	1.035	8.241	0.02554	510.5	7.429	13.6	1
	105	40.31	0.8974	0.760	5.023	0.009163	329.2	10.25	12.67	1
	120	44.54	0.8993	0.683	4.992	0.009323	271.1	11.24	11.87	1

For the SA sample, the initial values of R_b are higher than those in ASA due to the thicker barrier layer. The calculated initial thickness of barrier layer is 4.0 nm. However, values of R_b decrease to the similar level after 90 min of immersion. As a consequence, it can be concluded that the absorption of adipic species ($\text{H}_2\text{C}_6\text{H}_8\text{O}_4$, $\text{HC}_6\text{H}_8\text{O}_4^-$ or $\text{C}_6\text{H}_8\text{O}_4^{2-}$) in the porous layer inhibits the corrosion rate of barrier layer.

The ASA sample shows lower values of C_d , confirming that the adipic acid plays a block role during immersion. Accordingly, the process of mass transfer as well as ion migration (Al^{3+} or Cu^{2+} dissolved from the substrate) is also limited. For the ASA electrolyte, sulfuric acid is fully dissociated, while the dissociation constants for adipic acid are given by $K_1=3.8\times 10^{-5}$ and $K_2=3.9\times 10^{-6}$, respectively. Thus, the amount of adipic anions available in the solution during anodizing process is negligible. As a consequence, agent absorbed at the barrier layer / electrolyte interface is most probably in the form of $\text{H}_2\text{C}_6\text{H}_8\text{O}_4$. Moreover, electrochemical oxidation of aluminum is believed to result in the oxidation of hydrogenated amorphous carbon in the aqueous solution of adipic acid electrolyte. It is linked to the oxide network through the carboxylate ions and coordinative polyhedra of Al^{3+} and Cu^{2+} ions [30].

Based on the discussion above, a scheme of the mechanism is proposed (Fig. 8). During anodizing

process, adipic acid is absorbed in the porous layer in molecule form. Mass transfer (Al^{3+} or Cu^{2+} dissolved from the substrate) is influenced by the natural properties of carboxylic acid, thus, the film is uniform and regular. Meanwhile, the chemical dissolution of anodic layer, especially the barrier layer, is also suppressed at the barrier layer/electrolyte interface. After sealing process, more compact and thicker anodic film provides better inhibition to the penetration of aggressive ions. Moreover, the adipic species could be bidentate ligand capable of forming strong surface complexes with metallic ions (Al^{3+} and Cu^{2+}) that could chelate with metallic ions to inhibit further corrosion.

4 Conclusions

1) During anodizing, the adipic acid is absorbed in the porous layer, which helps the proton transmission in the electrolyte and prevents chemical dissolution of anodic layer.

2) With the addition of adipic acid, the film is uniform and compact especially at the film/substrate interface and the film thickness also increases.

3) After sealing procedure, anodic film formed with the addition of adipic acid exhibits improved dielectric property and corrosion resistance in aggressive environment.

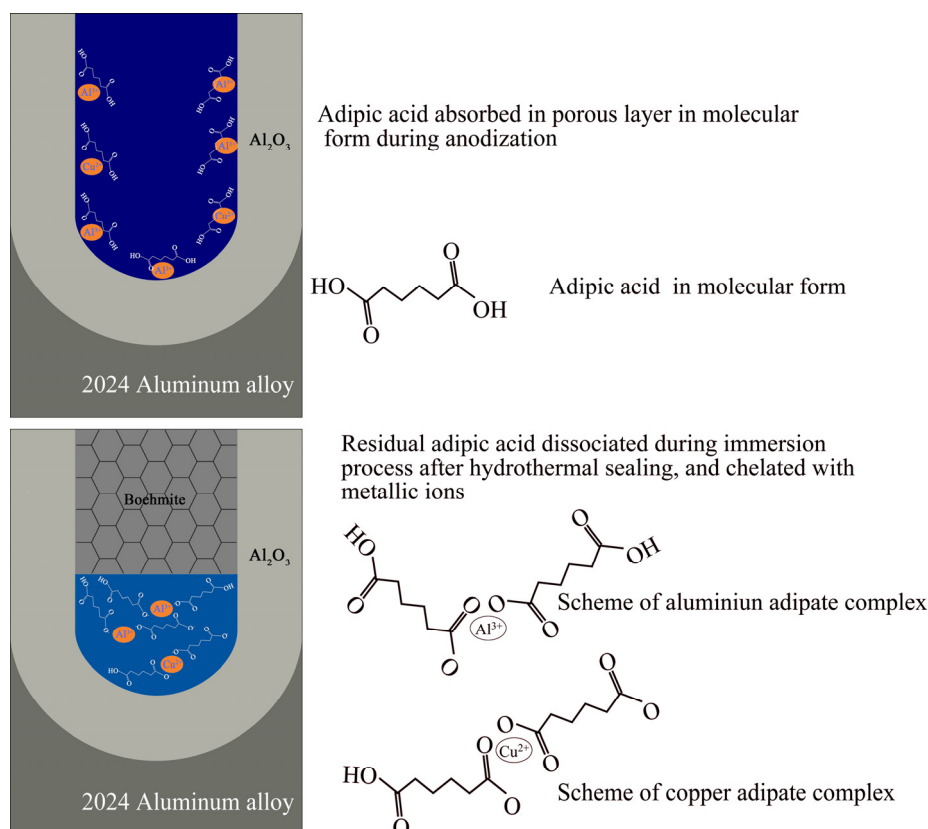


Fig. 8 Schematic diagram of proposed adsorption mechanism of adipic acid

References

- [1] MIRZAEI M, ROSHAN M R, JAHROMI S A J. Microstructure and mechanical properties relation in cold rolled Al 2024 alloy determined by X-ray line profile analysis [J]. *Materials Science and Engineering A*, 2015, 620: 44–49.
- [2] DEROSE J A, SUTER T, BALKOWIEC A, MICHALSKI J, KURZYDŁOWSKI K J, SCHMUTZ P. Localised corrosion initiation and microstructural characterisation of an Al 2024 alloy with a higher Cu to Mg ratio [J]. *Corrosion Science*, 2012, 55(2): 313–325.
- [3] WANG B B, WANG Z Y, HAN W, KE W. Atmospheric corrosion of aluminium alloy 2024-T3 exposed to salt lake environment in Western China [J]. *Corrosion Science*, 2012, 59(6): 63–70.
- [4] LIN Y C, JIANG Y Q, XIA Y C, ZHANG X C, ZHOU H M, DENG J. Effects of creep-aging processing on the corrosion resistance and mechanical properties of an Al–Cu–Mg alloy [J]. *Materials Science and Engineering A*, 2014, 605(5): 192–202.
- [5] NIE B, ZHANG Z, ZHAO Z, ZHONG Q. Effect of anodizing treatment on the very high cycle fatigue behavior of 2A12-T4 aluminum alloy [J]. *Materials & Design*, 2013, 50: 1005–1010.
- [6] DU Nan, WANG Shui-xing, ZHAO Qing, SHAO Zhi-song. Effects of boric acid on microstructure and corrosion resistance of boric/sulfuric acid anodic film on 7050 aluminum alloy [J]. *Transactions of Nonferrous Metals Society of China*, 2012, 22(7): 1655–1660.
- [7] DOMINGUES L, FERNANDES J C S, BELO C, FERREIRA M G S, GUERRA-ROSA L. Anodising of Al 2024-T3 in a modified sulphuric acid/boric acid bath for aeronautical applications [J]. *Corrosion Science*, 2003, 45(1): 149–160.
- [8] KIKUCHI T, NAKAJIMA D, KAWASHIMA J, NATSUI S, SUZUKI R O. Fabrication of anodic porous alumina via anodizing in cyclic oxocarbon acids [J]. *Applied Surface Science*, 2014, 313(13): 276–285.
- [9] KIKUCHI T, YAMAMOTO T, NATSUI S, SUZUKI R O. Fabrication of anodic porous alumina by squaric acid anodizing [J]. *Electrochimica Acta*, 2014, 123(10): 14–22.
- [10] QIN X F, ZHANG J Q, MENG X J, WANG L F, DENG C H, DING G Q, ZENG H, XU X H. Effect of ethanol on the fabrication of porous anodic alumina in sulfuric acid [J]. *Surface and Coatings Technology*, 2014, 254: 398–401.
- [11] ZARASKA L, SULKA G D, JASKUŁA M. The effect of *n*-alcohols on porous anodic alumina formed by self-organized two-step anodizing of aluminum in phosphoric acid [J]. *Surface and Coatings Technology*, 2010, 204(11): 1729–1737.
- [12] MOHAMMADI M, YAZDANI A, BAHROLOLOOM M E, ALFANTAZI A. Corrosion behavior of 2024 aluminum alloy anodized in presence of permanganate and phosphate ions [J]. *Journal of Coatings Technology and Research*, 2013, 10(2): 219–229.
- [13] MOUTARLIER V, GIGANDET M P, NORMAND B, PAGETTI J. EIS characterisation of anodic films formed on 2024 aluminium alloy, in sulphuric acid containing molybdate or permanganate species [J]. *Corrosion Science*, 2005, 47(4): 937–951.
- [14] REN J, ZUO Y. The anodizing behavior of aluminum in malonic acid solution and morphology of the anodic films [J]. *Applied Surface Science*, 2012, 261(1): 193–200.
- [15] CAPELOSSI V R, POELMAN M, RECLOUX I, HERNANDEZ R P B, MELO H G D, OLIVIER M G. Corrosion protection of clad 2024 aluminum alloy anodized in tartaric–sulfuric acid bath and protected with hybrid sol–gel coating [J]. *Electrochimica Acta*, 2014, 124(4): 69–79.
- [16] NAKAJIMA D, KIKUCHI T, NATSUI S, SUZUKI R O. Growth behavior of anodic oxide formed by aluminum anodizing in glutaric and its derivative acid electrolytes [J]. *Applied Surface Science*, 2014, 321: 364–370.
- [17] KIKUCHI T, YAMAMOTO T, SUZUKI R O. Growth behavior of anodic porous alumina formed in malic acid solution [J]. *Applied Surface Science*, 2013, 284(10): 907–913.
- [18] KAO T T, CHANG Y C. Influence of anodization parameters on the volume expansion of anodic aluminum oxide formed in mixed solution of phosphoric and oxalic acids [J]. *Applied Surface Science*, 2014, 288(1): 654–659.
- [19] DIMOGERONTAKIS T, TSANGARAKI-KAPLANOGLU I. The influence of certain sulfonic triphenylmethane dyes, as additives, on anodizing of aluminum in phosphoric acid [J]. *Thin Solid Films*, 2001, 385(1): 182–189.
- [20] WOJCIECH J S, DOMINIKA F, MALGORZATA N, MARTA M D, ARTUR K. The impact of viscosity of the electrolyte on the formation of nanoporous anodic aluminum oxide [J]. *Electrochimica Acta*, 2014, 133(7): 57–64.
- [21] CURIONI M, SKELDON P, KOROLEVA E, THOMPSON G E, FERGUSON J. Role of tartaric acid on the anodizing and corrosion behavior of AA 2024 T3 aluminum alloy [J]. *Journal of the Electrochemical Society*, 2009, 156(4): C147–C153.
- [22] MARZOCCHI V, IGLESIAS-RUBIANES L, THOMPSON G E, BELLUCCI F. The influence of tartaric acid additions on the anodizing behaviour of AA2024-T3 alloy in sulphuric acid [J]. *Corrosion Reviews*, 2011, 25(3–4): 461–473.
- [23] ARENAS M A, CONDE A, de DAMBORENEA J J. Effect of acid traces on hydrothermal sealing of anodising layers on 2024 aluminium alloy [J]. *Electrochimica Acta*, 2010, 55(28): 8704–8708.
- [24] BENSALAH W, FEKI M, WERY M, AYEDI H F. Chemical dissolution resistance of anodic oxide layers formed on aluminum [J]. *Transactions of Nonferrous Metals Society of China*, 2011, 21(7): 1673–1679.
- [25] SULKA G D, MOSHCHALKOV V, BORGHS G, CELIS J P. Electrochemical impedance spectroscopic study of barrier layer thinning in nanostructured aluminium [J]. *Journal of Applied Electrochemistry*, 2007, 37(7): 789–797.
- [26] MOON S M, PYUN S I. The mechanism of stress generation during the growth of anodic oxide films on pure aluminium in acidic solutions [J]. *Electrochimica Acta*, 1998, 43(21): 3117–3126.
- [27] KOBOTIATIS L, PEBERE N, KOUTSOUKOS P G. Study of the electrochemical behaviour of the 7075 aluminum alloy in the presence of sodium oxalate [J]. *Corrosion Science*, 1999, 41(5): 941–957.
- [28] LI L F, DAERDEN M, CAENEN P, CELIS J P. Electrochemical behavior of hot-rolled 304 stainless steel during chemical pickling in HCl-based electrolytes [J]. *Journal of the Electrochemical Society*, 2006, 153(5): B145–B150.
- [29] SREEKANTH D, RAMESHBABU N, VENKATESWARLU K. Effect of various additives on morphology and corrosion behavior of ceramic coatings developed on AZ31 magnesium alloy by plasma electrolytic oxidation [J]. *Ceramics International*, 2012, 38(6): 4607–4615.
- [30] VRUBLEVSKY I A, CHERNYAKOVA K V, ISPAS A, BUND A, ZAVADSKI S. Optical properties of thin anodic alumina membranes formed in a solution of tartaric acid [J]. *Thin Solid Films*, 2014, 556(4): 230–235.

己二酸对 2024 铝合金阳极氧化成膜和耐蚀性能的影响

李英东^{1,2}, 张 优¹, 李松梅¹, 赵丕植²

1. 北京航空航天大学 材料科学与工程学院, 北京 100191;

2. 中铝科学技术研究院有限公司, 北京 102209

摘 要: 研究己二酸对 2024 铝合金阳极氧化膜层形成及膜层耐蚀性能的影响。采用扫描电子显微镜(SEM)和透射电子显微镜(TEM)对膜层的形貌进行表征, 采用电化学阻抗谱(EIS)对膜层的耐蚀性能进行研究。结果显示, 在阳极氧化过程中, 己二酸在槽液/氧化膜界面产生吸附, 使膜层溶解速度降低、膜层厚度增加, 并且膜层结构更加均匀致密, 特别是在膜层/基体界面, 膜层的规整性得到改善。经过封闭处理后, 在添加己二酸的阳极氧化槽液中形成的膜层具有更加优异的介电性能, 在腐蚀性环境中具有更好的耐蚀性能。

关键词: 铝合金; 阳极氧化; 己二酸; 吸附; 腐蚀

(Edited by Wei-ping CHEN)